International Journal of Biological Macromolecules 369 (2026) 152684

Contents lists available at ScienceDirect

International Journal of Biological Macromolecules

journal homepage: www.elsevier.com/locate/ijbiomac

The [2Fe—2S] cluster and active-site architecture of *Corynebacterium diphtheriae* coproporphyrin ferrochelatase: Structure, stability, and catalysis

Alice Cassiani [a], Thomas Gabler [a], Andrea Dali [b], Paul G. Furtmüller [a], Federico Sebastiani [b,c,d], Maurizio Becucci [b,c,d], Giulietta Smulevich [b,c,*], Stefan Hofbauer [a,*]

[a] *BOKU University, Department of Natural Sciences and Sustainable Resources, Institute of Biochemistry, Muthgasse 18, A-1190, Vienna, Austria*
[b] *Dipartimento di Chimica "Ugo Schiff" (DICUS), Università di Firenze, Via della Lastruccia 3-13, I-50019, Sesto Fiorentino, FI, Italy*
[c] *INSTM, Research Unit of Florence, Via della Lastruccia 3, I-50019, Sesto Fiorentino, FI, Italy*
[d] *The European Laboratory for Non-Linear Spectroscopy (LENS), Via N. Carrara 1, I-50019, Sesto Fiorentino, FI, Italy*

ARTICLE INFO

Keywords:
Iron-sulfur cluster protein
ferrochelatase
Resonance Raman spectroscopy

ABSTRACT

Iron ferrochelatases (fCs) catalyse the insertion of ferrous iron into porphyrins. In the coproporphyrin-dependent heme biosynthesis pathway, utilized by Gram-positive bacteria, ferrochelatases are responsible for the penultimate step, yielding ferric iron coproporphyrin III (coproheme) starting from coproporphyrin III. Some representative fCs carry a [2Fe—2S] cluster, like the coproporphyrin ferrochelatase (CpfC) from the actinobacterium *Corynebacterium diphtheriae* (*Cd*). The general role of the iron-sulfur cluster, whether catalytic or else, is still unclear. Thus, we have studied (i) the structure of the protein and the [2Fe—2S] cluster coordination in detail by UV–vis electronic absorption and resonance Raman spectroscopies as well as by solving the X-ray crystal structure of apoprotein (apo) – WT *Cd*CpfC; (ii) active site variants to elucidate the role of a conserved distal histidine and glutamate pair for iron insertion and stabilization of the heme cavity.

Our results show that the iron-sulfur cluster is stably coordinated and that the type of the cluster, the nature of the ligands and the coordination motif are similar to those of human fC. The investigation of active site variants allows for a comprehensive comparison of the roles of conserved distal residues with those in previously studied coproporphyrin ferrochelatases from Firmicutes.

1. Introduction

Heme *b* is a nearly ubiquitous cofactor involved in many biological processes. Most organisms, which require heme to survive, are able to synthesize it [1,2]. Eukaryotes and diderm bacteria predominantly use the long known protoporphyrin-dependent (PPD) pathway, while monoderm bacteria, namely Firmicutes and Actinobacteria, utilize the coproporphyrin-dependent (CPD) pathway [3]. A third route, called siroheme-dependent (SHD) pathway, is only found in sulphate reducing bacteria and archaea [4,5]. Details on CPD and PPD pathways can be found in the literature [2,6–9]. In both the PPD and CPD pathways, the incorporation of ferrous iron into tetrapyrrole macrocycles is fundamental and catalysed by homologous enzymes, respectively protoporphyrin ferrochelatases (PpfC) and coproporphyrin ferrochelatases (CpfC). These ferrochelatases (fCs) have different physiological substrates: PpfC, as the last enzyme of the PPD pathway, converts protoporphyrin IX (ppIX) into iron protoporphyrin IX (heme *b*), while CpfC inserts Fe^{2+} ions into coproporphyrin III (cpIII) yielding ferric-coproporphyrin III (coproheme). Eventually, in the last step of the CPD pathway, the propionyl groups in positions 2 and 4 of coproheme are decarboxylated by coproheme decarboxylase (ChdC) to two vinyl groups, leading to heme *b* formation [1,2,6,10–12]. The metal insertion represents a key regulatory step for heme *b* biosynthesis, posing as the intersection point between iron supply chain and porphyrin synthesis [3,6]. Moreover, it was observed that low ferrochelatase activity causes the accumulation of toxic porphyrin in the cell [13] and leads to the insurgence of several diseases [14,15].

Prior to the identification of the CPD pathway, investigations on fCs from Gram-positive bacteria, were conducted assuming that these enzymes belong to the PPD pathway and, therefore, using two-propionate porphyrins instead of four-propionate cpIII as substrate. Nevertheless, the studies on CpfC from *Bacillus subtilis* with non-physiological substrates still provide significant information regarding metal binding and porphyrin deprotonation sites [16–19]. After 2015 [3], biochemical

* Corresponding authors.
E-mail addresses: giulietta.smulevich@unifi.it (G. Smulevich), stefan.hofbauer@boku.ac.at (S. Hofbauer).

https://doi.org/10.1016/j.ijbiomac.2026.152684
Received 6 March 2026; Received in revised form 15 May 2026; Accepted 22 May 2026
Available online 24 May 2026

investigations of CpfC from another Firmicute, *Staphylococcus aureus*, with coproporphyrin III highlighted the relation between a surface-exposed glutamate residue and the iron-mediated substrate inhibition in solution [20,21]. Recently, we have investigated the CpfC from *Listeria monocytogenes* (*Lm*CpfC) obtaining its X-ray crystallographic structure in the three relevant physiological forms (apo, coproporphyrin III- and coproheme- bound) [22,23]. Site-directed variants of *Lm*CpfC, aiming at residues involved in the coordination of propionates of both substrate and product, were used to investigate the H-bonding interactions in the active site pocket [8]. The importance of the hydrogen bonding network, between the four propionate groups of the physiological substrate or product and the protein, in the stabilization of the enzyme active site and catalysis was therefore demonstrated [8,23,24]. Additionally, we have also investigated the role of the key distal histidine-glutamate conserved pair (namely, His182 and Glu263 residues in *Lm*CpfC) and proximal not-conserved residue (Tyr12 in *Lm*CpfC) in the active site [25,26].

Among fCs, some contain a [2Fe—2S] cluster whose exact function is still under investigation [27]. Human PpfC is a homodimer membrane protein containing in each subunit a [2Fe—2S] cluster coordinated by one cysteine in the internal core of the protein and three cysteines in the external C-terminal region [28,29]. The cluster is suggested to be involved in the dimer stabilization and its removal results in a loss of activity [30,31]. However, the exact physiological role of the [2Fe—2S] cluster in human ferrochelatase and the reason for the observed loss of activity remains poorly understood. Possibly the lability of the cluster is connected to its function. For instance, by having an NO-sensing role, the cluster disassembles upon binding NO and loses activity [32]. Differently only some bacterial ferrochelatases have a [2Fe—2S] cluster. These cluster can be bound by four-cysteines coordinating motif in the C-terminal extension, similar to human PpfC, or by a cysteine-enriched internal insertion in the core region [33]. A recent study assessing the distribution of [2Fe-2S] cluster motif in available ferrochelatases genomic sequences, show that the cluster is completely missing in firmicute CpfCs and it is only present in a fraction of actinobacterial CpfCs, which display the same cysteine motif in the C-terminal extension as human PpfC [27]. However, the function of prokaryotic clusters is still elusive and, to our knowledge, it was only experimentally investigated prior to the discovery of the CPD pathway. In these studies, it was observed that microbial ferrochelatase [2Fe—2S] clusters are more stable than mammalian clusters under aerobic conditions. They are not destroyed by NO and are not essential for activity, although unusually low enzymatic activity of the actinobacterial ferrochelatase from *M. tuberculosis* was briefly mentioned [33,34]. Fe—S clusters can serve enzymatic reactions in many ways, like by stabilizing an intermediate, or being the entry point for other catalytic sites, without being involved in reduction and oxidation processes themselves [35–37].

Here, we present the first in-depth study of actinobacterial CpfC from *C. diphtheriae,* possessing a [2Fe—2S] cluster, with its physiological substrate (cpIII) and product (coproheme) by UV–vis electronic absorption and RR spectroscopies together with the determination of ligand binding constants and kinetics. Selected variants have also been investigated to elucidate the role of conserved distal residues in the active site. Further, an X-ray crystallographic structure of apo – WT *Cd*CpfC ('apo' with respect to the porphyrin-free structure, the iron-sulfur cluster is present) is presented and compared with the already available data on CpfC from *L. monocytogenes* in the apo-form and bound to coproheme and coproporphyrin III [22,23].

2. Materials and methods

2.1. Cloning, expression and purification of CdCpfC and variants

The genomic DNA encoding for *Cd*CpfC was incorporated via Gibson assembly into pET21(+) vector, equipped with ampicillin resistance gene and a C-terminal 6 × His-Tag for metal chelate affinity chromatography. Primers were designed for site directed mutagenesis to obtain the H197A and H286Q variants. The DNA fragments were amplified with PCR and assembled in same vector with Gibson assembly. All plasmids were transformed in *E. coli* XL-10 by heat-shock transformation and the cells were plated on selective agar plates. Positive clones were inoculated in LB media supplemented with 100 μg/mL ampicillin for overnight cultures, from which plasmids were purified with Monarch Plasmid MiniPrep Kit and sent for sequencing (Microsynth). Plasmids with the correct sequence were transformed by heat-shock transformation in the expression host *E. coli* BL21 Gold.

Expression was carried out at 37 °C in LB medium supplemented with 100 μg/mL ampicillin until an OD_{600} of 0.5–0.6. The cultures were cooled to 25 °C, induced with 0.35 mM IPTG and incubated at 20 °C overnight for expression. Cells were harvested by centrifugation (4500 rpm), resuspended in lysis buffer (20 mM PPi, 500 mM NaCl, 5% glycerol, 0.5% Titron X-100, 20 mM imidazole) and lysed by sonication (SONOPLUS Bandelin, Berlin, Germany). The cell debris were removed by centrifugation (18,000 rpm) and the lysate applied to an HisTrap column and eluted with imidazole gradient (20 mM–500 mM). The samples were purified by size-exclusion chromatography (Superdex 75, GE Healthcare) and stored in 1 × PBS with 100 mM NaCl, pH 7.4 at −80 °C. Protein concentration was confirmed by UV–vis spectroscopy (extinction coefficient 58,193 M^{-1} cm^{-1} at 280 nm).

2.2. Verification of monomeric state

The monomeric state of the enzymes was confirmed after each purification by HPLC (Shimadzu prominence LC20, Korneuburg, Austria), equipped with MALS (WYATT Heleos Dawn8 + plus QELS; software ASTRA 6, Dernbach, Germany), refractive index detector (RID-10A; Shimadzu), and a diode array detector (SPD-M20A; Shimadzu). The SEC column (Superdex 200 10/300 GL; GE Healthcare) with a particle size of 13 μm was equilibrated with 1 × PBS plus 200 mM NaCl. 80 μg of protein was loaded for each sample with a flow rate of 0.75 mL·min^{-1}. A sample of bovine serum albumin was used to verify the molar mass calculation by MALS, following the same method previously described [38].

2.3. Crystallization

Apo – WT *Cd*CpfC (10 mg·mL^{-1}) crystallized in optimized conditions of 15.182% *w/v* PEG8K, 0.04 M KH_2PO_4, 20% *v*/v glycerol within 8 days. Mosquito LCP (TTP Labtech, Melbourn, UK) was used to set drops on SWISSCI MRC three-well plates, testing three different ratios of protein (150 nL) to crystallization solution (100,150, 200 nL) with extra 100 nL of seeding solution (1:1000 dilution of harvested apo – WT LmCpfC crystals [22]). Crystals were fished and flash-vitrified in liquid nitrogen, no extra cryoprotection was necessary as the condition of crystal growth already contained 20% glycerol.

2.4. X-ray data collection, structure determination and refinement

Data for the apo – WT *Cd*CpfC data set was collected at the European Synchrotron Radiation Facility (Grenoble, France) at beamline ID23-1 at 100 K using an Eiger1 X 4M detector (doi.org/10.15151/ESRF-ES-537564077). The XDSAPP pipeline was used to process the data set.

Data quality assessment for the dataset was performed using Xtriage. The phase problem was solved by molecular replacement with PhaserMR using the pdb structure 6RWV of apo – WT *Lm*CpfC [22]. The initial models were generated with AUTOBUILD [39] and further improved by iterative cycles of manual model generation with COOT [40] and maximum likelihood refinement with PHENIX-refine [41]. The algorithm of French and Wilson [42] was used by PHENIX-refine to convert intensities to amplitudes. Finalization of the refinements included translation release screw (TLS) parameters, automatic addition of hydrogen and water molecules, optimization of the isotropic B-factor

model for X-ray/stereochemical weight, and optimization of X-ray/ADP weight. The model was validated using MolProbity [43] and by the pdb-redo server. Images were generated using PyMol (http://www.pymol.org).

2.5. UV–vis electronic absorption spectroscopy

A Cary 60 spectrophotometer (Agilent Technologies, Santa Clara, CA) was used to record UV–vis electronic absorption spectra in 1 mm or 10 mm quartz cuvette with scan rate of 300 nm·min^{-1} and a resolution of 1.5 nm. All spectra where registered between 250 and 700 nm. For the cpIII and coproheme complexes, the 450–700 nm region has been magnified, respect to the intensity of the Soret band, by a factor of 5–10, as indicated in the Figures.

2.6. Resonance Raman spectroscopy

The Resonance Raman spectra were obtained using the following laser excitation lines: 404.8 nm, diode laser (MatchBox Series, Integrated Optics, Vilnius, Lithuania); 441.6 nm, He—Cd laser (Kimmon IK4121R-G, Tokyo, Japan); 457 nm, diode laser (Cobolt Twist 200, Solna, Sweden); 532 nm, diode laser (Cobolt Samba 300, Hübner Photonics, Solna, Sweden). The backscattered light was collected and focused into a triple spectrometer. This consists of two monochromators (SpectraPro 2300i, Acton Research Corp., Acton, MA, USA) working in the subtractive mode and a SpectraPro 2500i instrument (Acton Research Corp., Acton, MA, USA) with gratings of 1800 and 3600 grooves/mm, with a nominal resolution of 4 and 1.2 cm^{-1}, respectively, equipped with a liquid nitrogen-cooled CCD detector. The room temperature experiments were performed at 298 K putting the sample (concentration 30 and 150 μM for holo- and apo- proteins, respectively) in 5 mm NMR tubes kept in slow rotation and UV–visible spectra were recorded before and after R measurement to ensure no degradation occurred. For the low temperature experiments, 50 μL droplet of the sample (300 μM) was put in a 1.5 cm diameter quartz crucible inside a THMS600 cryostat (Linkam Scientific Instruments, Surrey, UK) and frozen at 80 K. Indene and carbon tetrachloride were used as standard to calibrate the RR spectra to an accuracy of 1 cm^{-1}. To ensure reproducibility and optimize the signal-to-noise ratio, all RR measurements were repeated several times under the same experimental conditions and then all the spectra were averaged, when no spectral changes were observed, to improve the signal-to-noise ratio. Table S1 reports the laser power on the sample, integration time and number of averaged spectra in the figure. All spectra where baseline corrected. Since all the apo-protein spectra were obtained from the same sample in a single freezing cycle, the ice band at 221 cm^{-1} served as an internal standard to measure the Raman excitation profile at 80 K. We assumed the same relative Raman intensities at 80 K and 298 K. Differently, normalization of the spectra of the holo-proteins was performed on the most intense band in the spectra (i.e. the ν_4 band) and the 290–425 cm^{-1} region has been magnified, with respect to the intensity of the ν_4 band, by a factor of 2–15, as indicated in the figures.

2.7. Binding of CdCpfC to coproporphyrin III, coproheme and protoporphyrin IX

Coproporphyrin III dihydrochloride, ferric coproheme chloride and protoporphyrin IX were purchased from Frontier Scientific, Inc. (Logan, UT, USA) as lyophilised powder and dissolved in 0.5 M NaOH. Apo – WT *Cd*CpfC was titrated to 3 μM solution of substrate coproporphyrin III (extinction coefficient 150,736 M^{-1} cm^{-1} at 393 nm [8]) in 50 mM HEPES buffer, pH 7.4. After each addition UV–vis spectrum was recorded between 250 and 700 nm by a Cary 60 spectrophotometer (Agilent Technologies, Santa Clara, CA). The same method was applied for coproheme (128,800 M^{-1} cm^{1} at 390 nm [44]) and protoporphyrin IX (86,168 M^{-1} cm^{-1} at 373 nm [8]).

2.8. Enzymatic activity and content analysis by mass spectrometry

The insertion of ferrous iron into coproporphyrin III and formation of coproheme mediated by *Cd*CpfC was monitored using a Cary 60 spectrophotometer (Agilent Technologies, Santa Clara, CA). An excess of protein was bound to coproporphyrin III to ensure complete binding. A 100 mM ferrous iron stock solution was prepared under anaerobic conditions by dissolving in iron(II) sulphate heptahydrate (CAS: 7782-63-0; Sigma, Vienna, Austria) in Argon-degassed distilled and deionized water (ddH_2O) and adding DL-Dithiothreitol 1 M solution (CAS:3483-13-3; Sigma, Vienna, Austria) up to a 1:2 ratio, to keep the iron the ferrous form. From this stock a 1 mM ferrous iron solution was used for titration, performed anaerobically under argon flow. The same protocol was followed for H197A and E286Q variants. From this set-up, aliquots were taken from the cuvette and analysed by mass spectrometry as follows.

For each sample, 4 μL of solution was directly injected to a LC-ESI-MS system (LC: Agilent 1290 Infinity II UPLC). A gradient from 15 to 80% acetonitrile in 0.1% formic acid (using a Waters BioResolve column (2.1 × 5 mm) at a flow rate of 400 μL/min was applied (9 min gradient time). Detection was performed with a TOF instrument (Agilent Series 6230B) equipped with the Jetstream ESI source in positive ion, MS mode (range: 100–3200 Da). Instrument calibration was performed using ESI calibration mixture (Agilent). Data was processed using MassHunter BioConfirm B.08.00 (Agilent) and the spectrum was deconvoluted by BioConfirm B.08.00. Between each sample, there is a blank injected with a 6-min gradient time [44].

2.9. Kinetics of coproporphyrin III and coproheme binding to CdCpfC and of substrate conversion

Coproporphyrin III and coproheme time-resolved binding to apo – WT *Cd*CpfC was monitored by a stopped-flow apparatus equipped with a monochromator and a photomultiplier detector (model Pistar-180; Applied Photophysics, Leatherhead, UK) using an Hg/Xe lamp. The optical quartz cell with 10 mm pathlength had a volume of 20 μL. The fastest mixing time was between 1.0 and 1.5 ms. The ligand in the cell was kept at a constant concentration of 1 μM and the apo – WT *Cd*CpfC was added in excess in a range between 4.0 and 6.5 μM for coproporphyrin III and 4.5 and 7 μM for coproheme, to ensure complete formation of the ligand bound species. All measurements were carried out in 50 mM HEPES, pH 7.4 at 25 °C. Time traces recorded in triplicates at a single wavelength, 404 nm for coproporphyrin III and 390 nm for coproheme, were fitted double and single exponentially, respectively. The obtained k_{obs} values were plotted versus *Cd*CpfC concentration to obtain the second-order rate constant k_{on} and the first-order rate constant k_{off}. The constants k_{on} and k_{off} constants where then used to calculate the dissociation constant K_D. The same method was used to monitor the time resolved conversion of coproporphyrin III to coproheme, mediated by WT *Cd*CpfC. A 10 mM ferrous iron stock solution was prepared under anaerobic conditions by dissolving in iron(II) sulphate heptahydrate (CAS: 7782-63-0; Sigma, Vienna, Austria) in Argon-degassed ddH_2O. An excess of protein was bound to coproporphyrin III to ensure complete binding. The substrate bound apo – WT *Cd*CpfC was kept at a constant concentration of 2 μM in the cell and ferrous iron was added in excess in a range between 4.25 and 6.5 μM. All measurements were carried out in argon-degassed 50 mM HEPES, pH 7.4 at 25 °C. The time traces recorded in triplicates at 404 nm were fitted double exponentially. The obtained k_{obs} values were plotted versus ferrous iron concentration to obtain the second-order rate constant k_{on}. The same method was applied for the H197A and E286Q *Cd*CpfC variants. However, the concentration range had to be increased to 100-220 μM.

3. Results

3.1. Structure of apo - CdCpfC

The diffraction data for apo – wild-type (WT) *Cd*CpfC were acquired with a resolution of 1.87 Å and the structure was solved by molecular replacement using apo – WT *Lm*CpfC. Complete data collection and refinement statistics are reported in Table 1.

Apo – WT *Cd*CpfC folds into a monomeric protein with two ferredoxin-like domains, similar to *Lm*CpfC (Fig. 1) [22]. Both domains consist of a four-stranded parallel β-sheet flanked by α-helices, building a cleft shown to be the substrate binding site in *Lm*CpfC. In addition, a ferredoxin-like [2Fe—2S] cluster is located in the C-terminal region, a feature not found in *Lm*CpfC. Each iron atom of the cluster is chelated by two bridging sulfide groups and two thiolate groups of cysteine residues. The cluster is coordinated by one internal cysteine (Cys127), connecting the site of the [2Fe—2S] cluster with the porphyrin binding pocket, and three proximal cysteines in C-terminal loop (Cys353, Cys357, Cys358). The two consecutive cysteines, Cys357 and Cys358, pair together and bind Fe_2, while Cys353 and Cys127 bind the other iron atom Fe_1. A similar cysteine motif (Cys-X_{206}-Cys-X_2-Cys-X_4-Cys) is found in dimeric human PpfC, but the clusters themselves do not align structurally (Fig. S1).

Both coproporphyrin III and coproheme contain four propionates in positions 2, 4, 6 and 7. They will be referred as p2, p4, p6 and p7, respectively, in the text. The architecture of active site of *Cd*CpfC is described by three key residues: the highly conserved His197/Glu286 pair (His182/Glu263 in *Lm*CpfC) in the distal site and Phe20 in the proximal site, which is a not conserved residue in ferrochelatases, being replaced by Tyr12 in *Lm*CpfC and Met76 in human PpfC [45] (Fig. 2A). Sequence alignment of *Cd* and *Lm* CpfCs revealed that not all residues involved in propionate H-bonding are conserved (Fig. 2B). For instance, in *Cd*CpfC Thr37 and His53 replace Arg29 and Arg45 of *Lm*CpfC, forming H-bonding interaction with p7 and p6 in *Lm*CpfC, respectively. Thr14 (in *Lm*CpfC numbering) is also replaced by Gly22, while the other two residues Tyr46 and Ser53 (in *Lm*CpfC numbering) involved in the H-bond network with p4 are conserved in *Cd*CpfC as Tyr54 and Ser61. The residue forming H-bond interaction with p2, Tyr124 and the proposed surface-exposed Fe-regulatory site [20], Glu271 (in *Lm*CpfC numbering), are also conserved in *Cd*CpfC as Tyr130 and Glu294, respectively (the site of Glu271/Glu294 is not shown in Fig. 2).

Structural comparison of apo WT -*Cd*CpfC with apo -, coproheme - and cpIII - bound WT *Lm*CpfC [8,22,23] shows some interesting differences in the structural arrangement of the binding cleft (Fig. 2B). Starting from the apo-CpfC structure the relevant residues for porphyrin binding are predicted on the basis of similarities and alignments with other porphyrin-bound CpfC structures. For instance, in *Cd*CpfC Glu286 shows less flexibility compared to the corresponding Glu263 in *Lm*CpfC, which is oriented away from His182 in the apo form. In the coproheme-*Lm*CpfC structure Glu263 is resolved in a split conformation, while Glu286 is only partially involved in H-bond with His197 in coproheme – WT *Cd*CpfC complex. Glu286 and His197 in apo – WT *Cd*CpfC are within H-bond distance (2.9 Å), mimicking the orientation of Glu263 and His182 in *Lm*CpfC bound to coproporphyrin III (Fig. 2A). Also, while the side chain of Ser53 in apo – WT *Lm*CpfC is solvent exposed, in apo – WT *Cd*CpfC the side chain of Ser61 is directed toward the protein core, as in the apo-forms of *Lm*CpfC. In *Cd*CpfC apo structure, Tyr54 and Tyr130 side chains are both directed toward the cleft core, and Gly22 is in close proximity and part of the active site, even if it is unlikely to be involved in H-bonding interaction with p4. On the contrary, Thr37 and His53 point away from the binding cleft, as Arg29 and Arg45 in the apo – WT *Lm*CpfC. Structural data from *Lm*CpfC suggest that the rearrangement of the side chain only occurs upon ligand binding. Interestingly, Arg40 in *Cd*CpfC has its side chain directed toward the protein inner core and is within H-bonding distance to p7, when we align apo – WT *Cd*CpfC with coproheme – or cpIII – WT *Lm*CpfC. Considering its location on a flexible loop, Arg40 could also be part of p7 H-bonding network, differently from the corresponding His32 (in *Lm*CpfC numbering) which is solvent exposed in all forms of *Lm*CpfC (Fig. 2B).

Table 1
Statistics of data collection and refinement of apo WT *Cd*CpfC (PDB ID: 28WN).

Wavelength (Å)	0.9677
Resolution range	46.98–1.872 (1.939–1.872)
Space group	P 21 21 2
Unit cell	66.233 133.286 45.17 90 90 90
Total reflections	442,473 (39382)
Unique reflections	33,195 (3035)
Multiplicity	13.3 (13.0)
Completeness (%)	98.22 (92.14)
Mean I/sigma(I)	10.21 (2.73)
Wilson B-factor	23.99
R-merge	0.1791 (0.828)
R-meas	0.1862 (0.8617)
R-pim	0.05032 (0.2348)
CC1/2	0.995 (0.854)
CC*	0.999 (0.96)
Reflections used in refinement	33,179 (3035)
Reflections used for R-free	1115 (102)
R-work	0.1730 (0.2579)
R-free	0.2022 (0.2712)
CC(work)	0.955 (0.836)
CC(free)	0.977 (0.859)
Number of non-hydrogen atoms	3124
Macromolecules	2790
Ligands	41
Solvent	305
Protein residues	354
RMS(bonds)	0.003
RMS(angles)	0.60
Ramachandran favored (%)	98.01
Ramachandran allowed (%)	1.99
Ramachandran outliers (%)	0.00
Rotamer outliers (%)	0.33
Clashscore	2.34
Average B-factor	26.21
Macromolecules	24.96
Ligands	41.05
Solvent	36.20

3.2. Characterization of apo - CdCpfC [2Fe2S] cluster

Purification of *Cd*CpfC and the two distal variants expressed in *E. coli* yielded ~100 mg of protein per liter of *E. coli* culture. Protein monodispersity was confirmed by HPLC-SEC-PDA-MALS and the determined average molecular weight of 43.8 kDa for *Cd*CpfC agrees with the theoretical value of 42.2 kDa (Fig. 3B). Similarly, *Cd*CpfC H197A and *Cd*CpfC E286Q average molecular weight is 42.4 kDA and 43.9 kDa. The UV–visible absorption spectrum of *Cd*CpfC (Fig. 3A) shows four Fe ← S ligand-to-metal charge transfer (LMCT) bands at 326, 409, 447 and 576 nm, typical of a $[2Fe—2S]^{2+}$ cluster [46] and similar to that of the human fC [28] (Table S2). In detail, the two bands at 409 and 447 nm can be attributed to the electronic transfer between the iron *3d* orbital and the σ orbitals of the bridging sulfur (μS) atom and are distinctive of a $[2Fe—2S]^{2+}$ clusters [47,48]. The remaining two bands at 326 nm and 576 nm can be assigned as Fe *3d* ← μS and Fe *3d* ← σ*-S, respectively, which are usually found around 330 nm and 550 nm, respectively [47,48]. In the region between 260 and 280 nm, bands due to electronic transfer between the iron 3d orbital and σ and *3p* non-bonding orbitals of the cysteine sulfur atom should be observed, but they are overlapped with the intense aromatic amino acid band at 280 nm. The cluster bands are also present in *Cd*CpfC H197A and E286Q (Fig. 3A) with similar spectroscopic characteristics. However, in the UV–visible absorption spectrum of the E286Q mutant, a band at 415 nm, not present in the spectra of the wild-type or the H197A mutant, is observed. This band is likely due to residual heme or a porphyrin derivative from the host *E. coli*. The presence of the 415 nm band likely obscures the cluster band

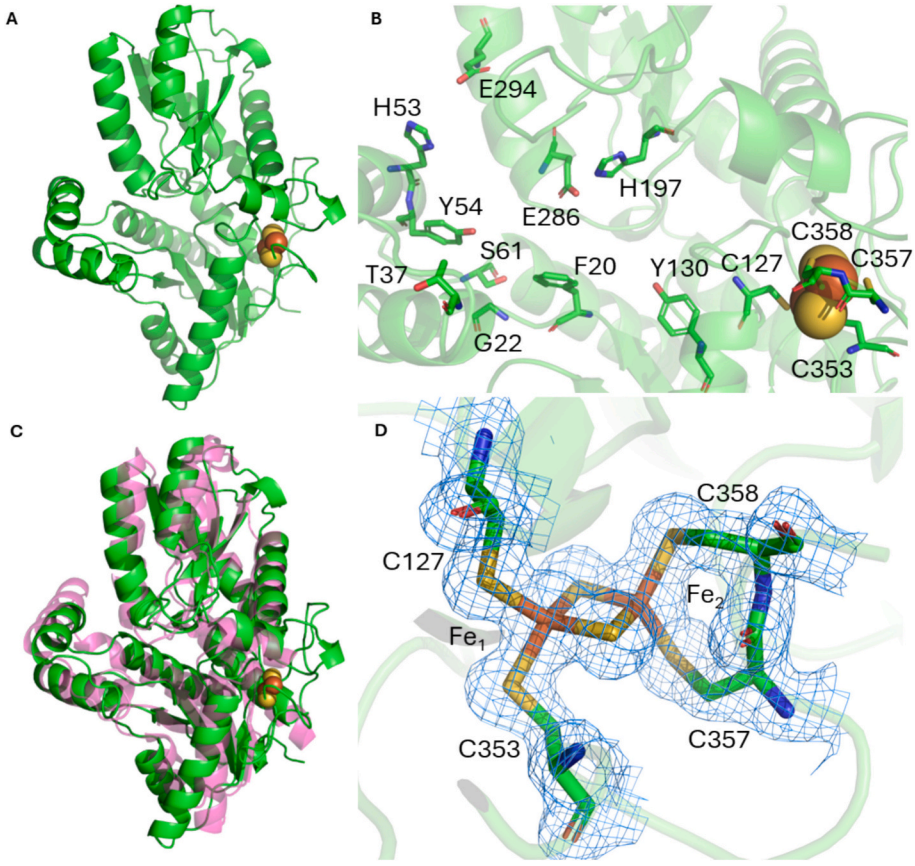

Fig. 1. (A) Overall structure of apo - WT *Cd*CpfC (PDB ID: 28WN) represented as a cartoon with key amino acids represented as sticks. (B) Close up of apo – WT *Cd*CpfC porphyrin binding site and iron-sulfur cluster binding site with key amino acids represented as sticks. (C) Overlay of apo – WT *Cd*CpfC (green) and apo – WT *Lm*CpfC (pink) (PDB ID: 6RWV) represented as cartoon. (D) Highlight of [2Fe-2S] cluster coordination motif overlaid with the 2mFo-DFc electron density map at 1σ.

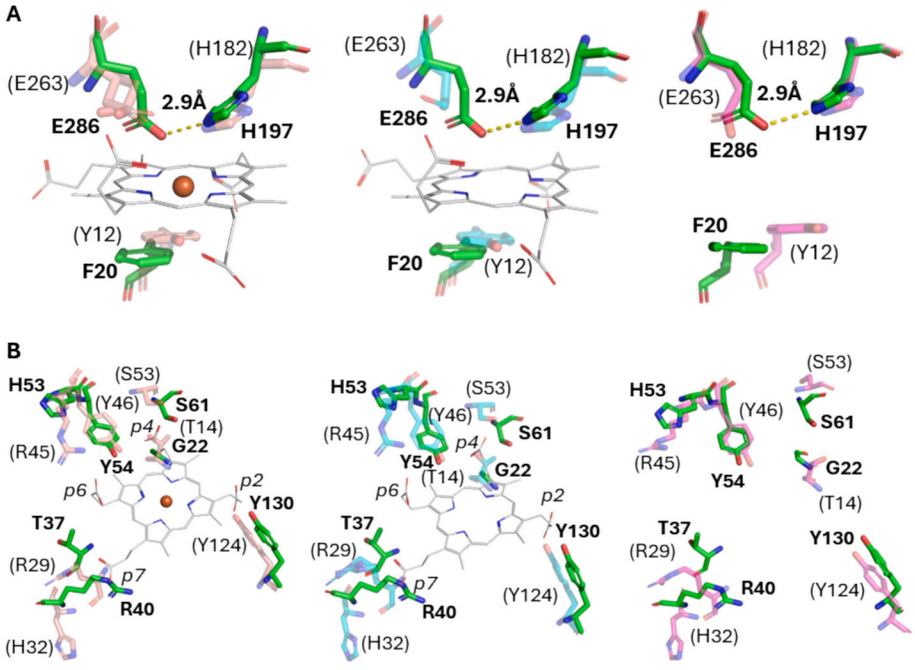

Fig. 2. (A) Architecture of distal and proximal active site in apo – WT *Cd*CpfC (green) (PDB ID: 28WN) overlaid with coproheme - (left, salmon) (PDB ID:6SV3), cpIII - (middle, cyan) (PDB ID: 8AT8) and apo – WT *Lm*CpfC (right, magenta) (PDB ID: 6RWV). (B) Stick representation of potential propionate binding residues in apo – WT *Cd*CpfC binding cleft overlaid with the corresponding residues in coproheme -, cpIII -, apo – WT *Lm*CpfC using the same colour code.

at 409 nm, which is typically weak, rather than indicating a shift in the cluster band.

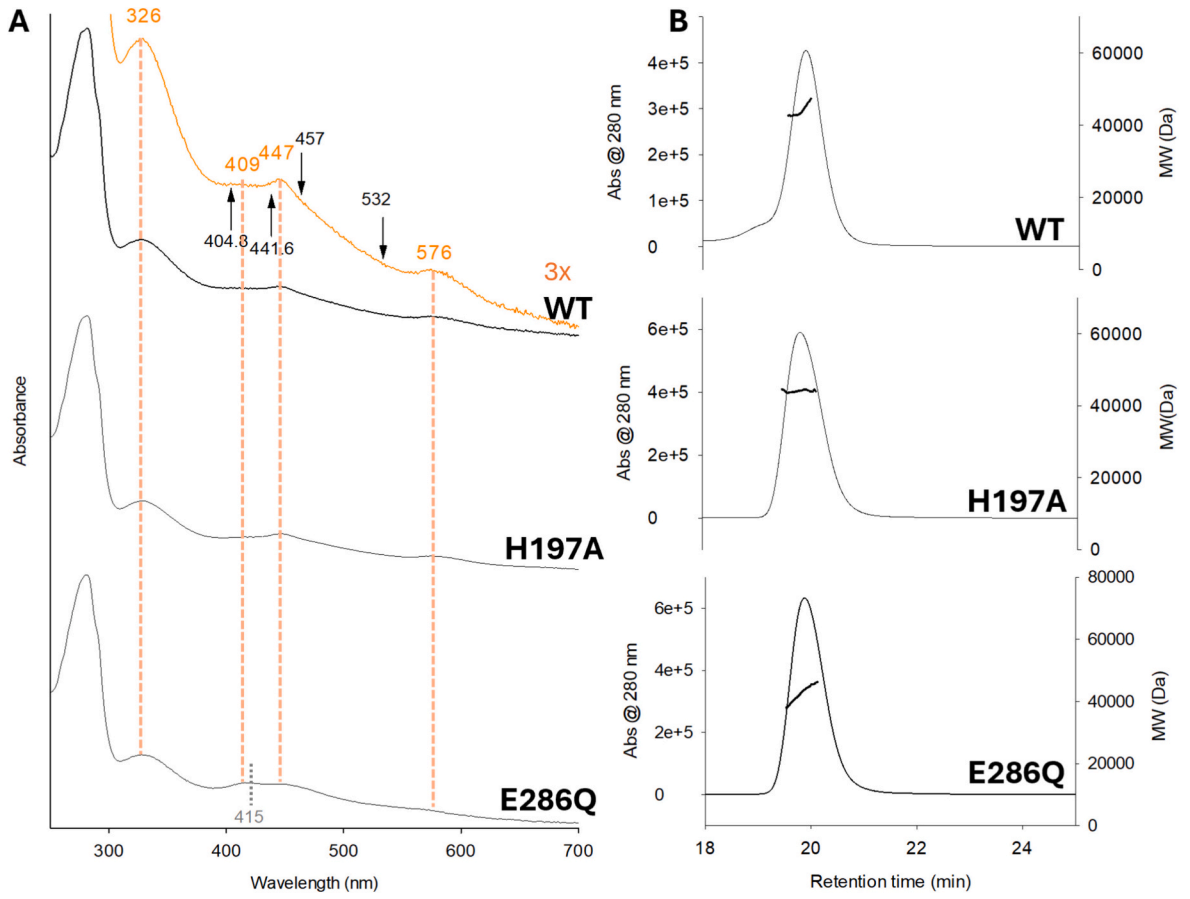

Fig. 3. (A) UV–visible electronic absorption spectrum of apo- WT *Cd*CpfC, and its H197A, and E286Q variants. For the WT apo it is represented also a threefold-scaled trace (orange) highlighting the [2Fe—2S] cluster bands. Black arrows show the chosen excitation wavelengths for resonance Raman experiments (see below). (B) HPLC-SEC-PDA profile of *Cd*CpfC and distal variants followed by UV–vis absorbance at 280 nm with black, bold lines across the absorption peak showing the molecular weight calculated via MALS detector.

Resonance Raman (RR) spectroscopy has been successfully used to study the structure of [2Fe-2S] clusters in proteins [49]. RR spectra obtained in resonance with the LMCT transitions of the Fe—S cluster result in the intensification of specific vibrational modes without interferences from the Raman bands of the apo-protein. These modes are identified by a superscript referring to the main internal coordinate contributor, stretching of the bridging (b) or terminal (t) Fe—S bonds involving the inorganic or the cystenyl sulfur atoms, respectively. In the 280–420 wavenumber region, the $(Fe—S)^b$ and the $(Fe—S)^t$ vibrational modes are observed [49–54]. In particular, the bridging modes are found in the 315–425 cm^{-1} range, while the terminal modes are in the 290–360 cm^{-1} region [55]. The wavenumbers of the Fe—S stretching vibrations allow one to distinguish among different Fe—S clusters and to identify the ligands coordinated to the iron atoms [30,49,52,53,55–59]. On the basis of the idealized D_{2h} point group of the 2Fe—2S cluster, the vibrations are classified in totally symmetric, A_g^b and A_g^t, and not totally symmetric modes, B_{1g}^b, B_{1u}^t, B_{2u}^b, B_{2g}^t, B_{3u}^b, B_{3u}^t [53,56]. To investigate the [2Fe—2S] observed in the crystallographic structure (Fig. 1) we obtained the Raman spectra of apo – WT *Cd*CpfC (Fig. 4) using different excitation wavelengths (404.8, 441.6, 457, 514.5, and 532 nm), i.e. working in resonance with the four Fe ← S LMCT bands at 326, 409, 447 and 576 nm (Fig. 3). Furthermore, to improve the spectral resolution the spectra were obtained both at room (298 K, Fig. 4A) and low temperatures (i.e. 80 K, Fig. 4B). The investigation of the cluster has been performed in its ferric form, since reduction was not possible, even at high concentration of sodium dithionite. To obtain information on the contribution of the different electronic states to Raman scattering, the excitation profile (EP), i.e. the variation of Raman intensity at 80 K as a function of the excitation wavelength, has been measured (Fig. 4C). Since all the sets of spectra were obtained from the same sample, the ice band at 221 cm^{-1} served as an internal standard as previously reported for other Fe—S cluster containing proteins [53,60].

The band at 383–384 cm^{-1} is assigned to A_g^b mode, following the assignment in bovine adrenodoxin [59]. In agreement with the study on oxidized putidaredoxin [59], the bands at 323–322 cm^{-1}, 329–328 cm^{-1} and 347–346 cm^{-1} are assigned to B_{1g}^b, A_g^t and B_{3u}^b modes, respectively. The near degenerate mode B_{1u}^t, B_{2g}^t modes are at 351–353 cm^{-1}, similar to the case of *P. umblilicalis* ferrodoxin [56]. Upon excitation at 532 nm at 80 K a single band a 349 cm^{-1} is observed, due to the overlapping of the bands at 346 (B_{3u}^b) and 353 cm^{-1} (B_{1u}^t, B_{2g}^t). Only the assignment of B_{3u}^t mode remains uncertain, as two bands at 280 and 288 cm^{-1} are observed at both temperatures, being intensified with the 404.8 and 532 nm excitations. Typically, clusters with complete cysteine coordination have a single band in the 280–295 cm^{-1} range. To the best of our knowledge, more than one B_{3u}^t modes are reported only for the mitoNEET, a mitochondrial membrane protein with a $[2Fe—2S]^{2+}$ cluster with a $(His)(Cys)_3$ coordination motif [61], where, a splitting into three or two B_{3u}^t modes was observed for the native protein or a mutant with a complete Cys coordination, respectively. The remaining unassigned bands at 312, 319, 398 and 412 cm^{-1} are too weak for determining their excitation profiles. In agreement with previously reported data [59], B_{1g}^b and B_{3u}^b modes are intensified upon excitation at 457 nm, while B_{1u}^t and B_{2g}^t modes are enhanced upon 404.8 nm excitation (Fig. 4C and Table S3). The A_g^b and A_g^t excitation profiles follow the absorption band intensity, being intensified upon 441.6 and 457 nm excitation respectively. In agreement with other Fe—S cluster proteins

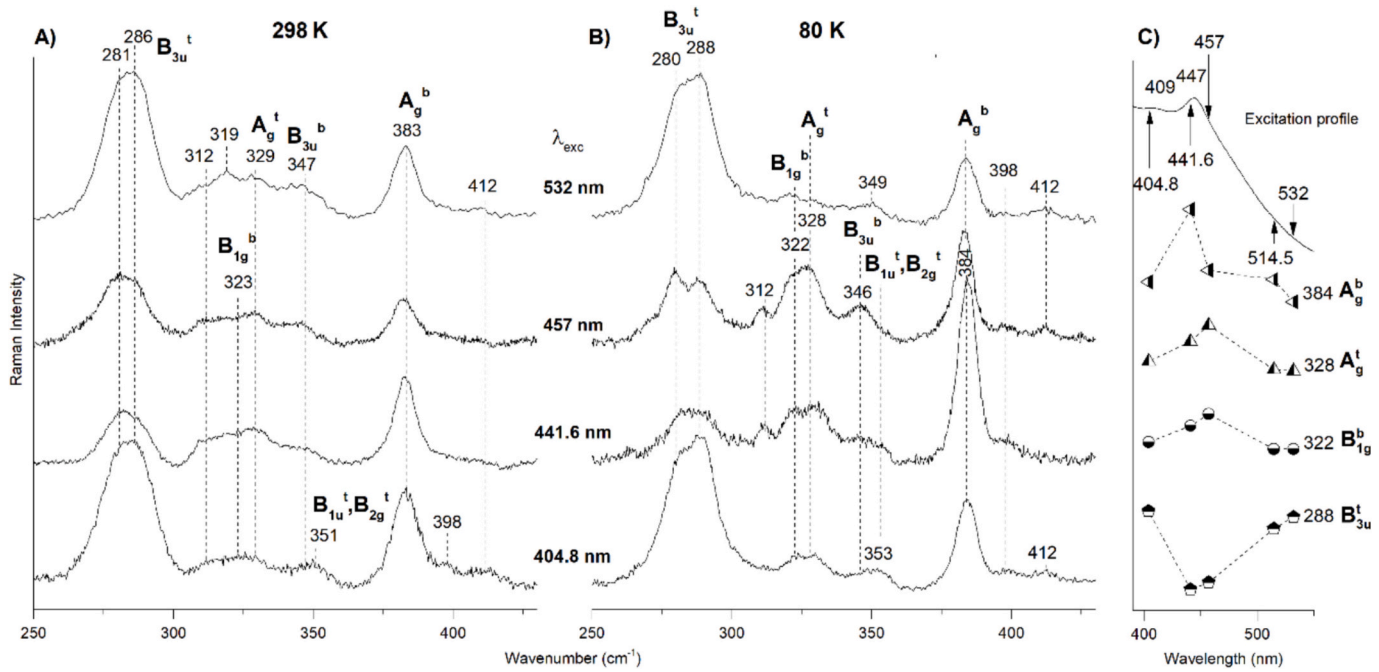

Fig. 4. (A) RR spectra in the low wavenumber region of apo - WT *Cd*CpfC obtained upon 404.8, 441.6, 457 and 532 nm excitation at room temperature and (B) at low temperature. The ice band at 221 cm^{-1} served as an internal standard. (C) RR excitation profile for selected bands wavenumbers (in cm^{-1}) at 80 K. The excitation profile is reported also upon 514.5 nm excitation (spectra not shown). The b and t superscripts indicate the vibrations of the bridging $(Fe—S)^b$ (involving inorganic sulfur) and the terminal $(Fe—S)^t$ (involving cysteinyl sulfur ligands), respectively.

[59], the very intense bands at 280–288 cm^{-1} (B^t_{3u}) and the bands at 328 (A^t_g) and 384 (A^b_g) cm^{-1}, observed in solution, confirm the presence of a $[2Fe—2S]^{2+}$ cluster with a complete cysteinyl coordination, as human fC [30]. Interestingly, while the type of the cluster, the nature of the ligands and the coordination motif are similar between human and *Cd* fCs [27], in the case of *Cd*CpfC the Fe—S stretching modes have different relative intensities and EP, as compared to the human fC (Table S3).

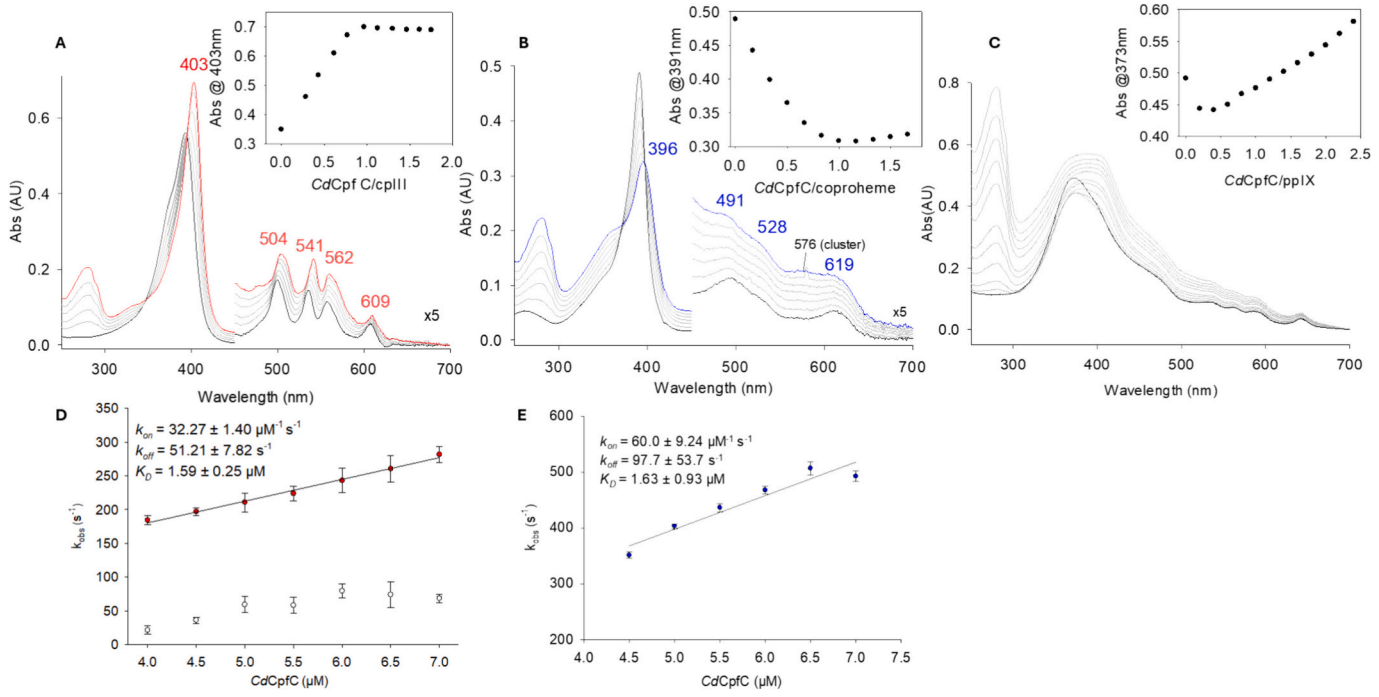

Fig. 5. UV–vis spectra of 3 μM cpIII (A) and coproheme (B) (black) titrated with WT *Cd*CpfC up to complete binding (red and blue trace, respectively), intermediate spectra are depicted as gray lines. The insets show the absorbance at 403 nm and 391 nm plotted versus the ratio *Cd*CpfC/cpIII and *Cd*CpfC/coproheme, respectively. (C) UV–vis spectra of ppIX titrated with *Cd*CpfC up to 2.5 eq shows no binding (only gray traces). The inset shows the absorbance at 373 nm plotted versus the ratio *Cd*CpfC/ppIX. Linear dependence of k_{obs1} of cpIII (red dots, D) and coproheme (blue dots, E) binding on increasing protein concentration and no correlation with k_{obs2} (with dots, D). Error bars represent the standard deviation calculated from three independent replicates.

3.3. Selectivity of CdCpfC ligand binding and binding kinetics

*Cd*CpfC ligand binding to its natural substrates, coproporphyrin III, and product, coproheme, as well as to the substrate of protoporphyrin ferrochelatases, ppIX, was followed by UV–vis spectroscopy (Fig. 5). *Cd*CpfC is able to bind both cpIII and coproheme with a 1:1 ratio. cpIII-*Cd*CpfC complex has a Soret maximum at 403 nm and Q bands at 504, 541, 563 and 610 nm (Fig. 5A, red trace), clearly shifted compared to the spectrum of free coproporphyrin III (Fig. 5A, black trace). Coproheme – WT *Cd*CpfC exhibits a Soret maximum at 396 nm, two Q bands at 491 and 528 nm and a charge transfer band at 614 nm, while only one of the cluster bands is visible at 576 nm (Fig. 5B, blue trace). These spectroscopic features are similar to those previously reported for *Lm*CpfC [22]. Differently from *Lm*CpfC, *Cd*CpfC is unable to bind ppIX even in a 2.5-fold excess (Fig. 5C), while the ppIX-*Lm*CpfC complex is characterized by a Soret at 412 nm and Q bands at 510, 548, 573, 626 nm [8].

In addition, coproporphyrin III binding kinetics show a biphasic behavior and time traces were fitted double exponentially. A linear dependence on the concentration of *Cd*CpfC was observed for k_{obs1}, resulting in $k_{on} = 32.27 \times 10^6\ M^{-1}\ s^{-1}$, $k_{off} = 51.21\ s^{-1}$ and $K_D = 1.59$ μM. On the other hand, coproheme binding shows a monophasic behavior and time traces were fitted single exponentially. For coproheme binding, the kinetic parameters were the following: $k_{on} = 60.0 \times 10^6\ M^{-1}\ s^{-1}$, $k_{off} = 97.7\ s^{-1}$ and $K_D = 1.63$ μM (Fig. 5D-E). The k_{on} rate for coproheme binding is higher than for cpIII binding, however, they are of the same order of magnitude and the k_{off} value of coproheme is also higher than for cpIII, which results in very similar K_D constants.

3.4. Spectroscopic characterization of WT CdCpfC

WT *Cd*CpfC complexed with cpIII shows spectroscopic features similar to those previously reported for *Lm*CpfC [23], both in the UV–vis (Fig. 6A, top) and RR spectra obtained upon Soret excitation (Fig. 6B-C, top). In fact, the activation of the out-of-plane modes (γ_7 and γ_6 at 322 and 353 cm^{-1}, respectively) indicate the same doming distortion of the porphyrin as in *Lm*CpfC (Fig. 6B), and very similar porphyrin core size marker bands (Fig. 6C), whose wavenumbers are reminiscent of those of a hexacoordinated high-spin (6cHS) metallo-protein. Although the region between 360 and 430 cm^{-1} is less resolved than that the corresponding of WT *Lm*CpfC, three propionate $\delta(C_\beta C_c C_d)$ bending modes are observed at 365, 385, 391 cm^{-1}. The fourth expected propionate bending mode is assigned at 405 cm^{-1}, as it is intensified upon 404.8 nm excitation wavelength.

Also upon binding of coproheme to WT *Cd*CpfC, the UV–vis spectra are very similar to *Lm*CpfC (Fig. 6A, bottom), characteristic of a penta-coordinated (5c) high-spin (HS) ferric porphyrin with a weak proximal ligand (as indicated by the similar intensity of the ν_3 at 1492 cm^{-1} and ν_4 at 1374 cm^{-1} bands, Fig. 6C), probably a water molecule [8]. The coproheme is stabilized inside the pocket by H-bond interactions between the propionate groups and polar residues of the protein, as indicated by the presence of four $\delta(C_\beta C_c C_d)$ propionate bending modes (367, 371, 387, 395 cm^{-1}) (Fig. 6B, bottom). The differences in terms of wavenumbers and intensities of these bands as compared to *Lm*CpfC, indicate different H-bond strengths between the porphyrin and the two protein scaffolds, as suggested by the overlay of the X-ray structures of the apo – WT *Cd*CpfC with the cpIII-*Lm*CpfC complex.

3.5. Effect of distal mutation: H197A and E268Q CdCpfC variants

Based on the interesting differences in the structural arrangement of the binding cleft suggested by the structural comparison of apo – WT *Cd*CpfC with apo-, coproheme- and cpIII-bound WT *Lm*CpfC (Fig. 2B), we have characterized the H197A and E268Q variants in order to assess the role of conserved distal residues in maintaining the active site structure and stability.

The UV–vis and RR spectra of the WT - cpIII complex are almost identical to those of the E268Q distal variant (Fig. 7) suggesting that mutation of the Glu268 residue does not significantly alter the heme pocket. The only differences are observed in the propionate $\delta(C_\beta C_c C_d)$ bending modes region. In fact, a shift in the bending mode wavenumbers (362, 382, 391 and 405 cm^{-1}) suggests a change of the interactions between the propionate groups and the protein pocket upon distal mutations. On the contrary, mutation of His197 with the apolar Ala residue markedly affects the UV–vis spectrum (Fig. 7A). The H197A-cpIII complex is characterized by a blue-shifted electronic absorption spectrum as compared to WT and E268Q variant. Analyzing the RR spectra it can be observed that, while the core size marker bands region is almost identical to that of the WT (Fig. 7C), major changes are observed in the low

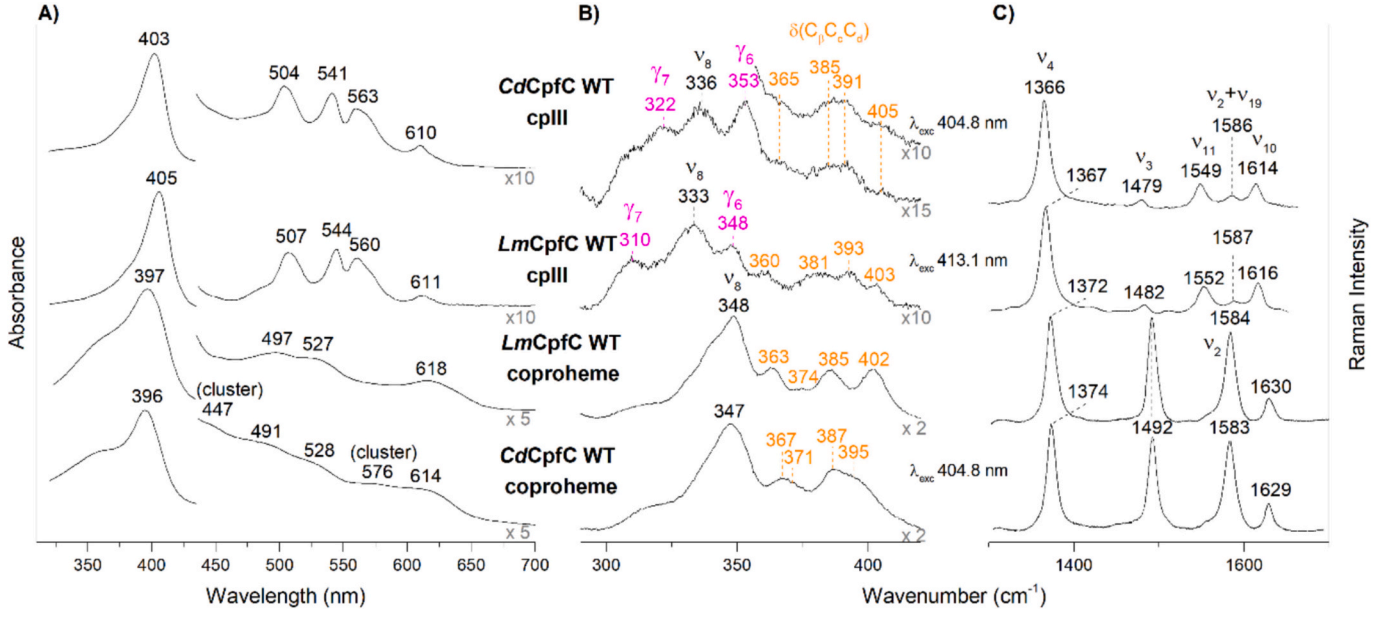

Fig. 6. (A) UV−vis absorption, and RR spectra in the low (B) and high (C) wavenumber region of cpIII – and coproheme - WT *Lm*CpfC and WT *Cd*CpfC obtained upon 404.8 nm (coproheme) and 404.8 and 413.1 nm (cpIII) excitation wavelengths. The propionates bending modes $\delta(C_\beta C_c C_d)$ wavenumbers are reported in orange and in purple the RR out-of-plane band wavenumbers. The *Lm*CpfC data are taken from Refs. [8,23].

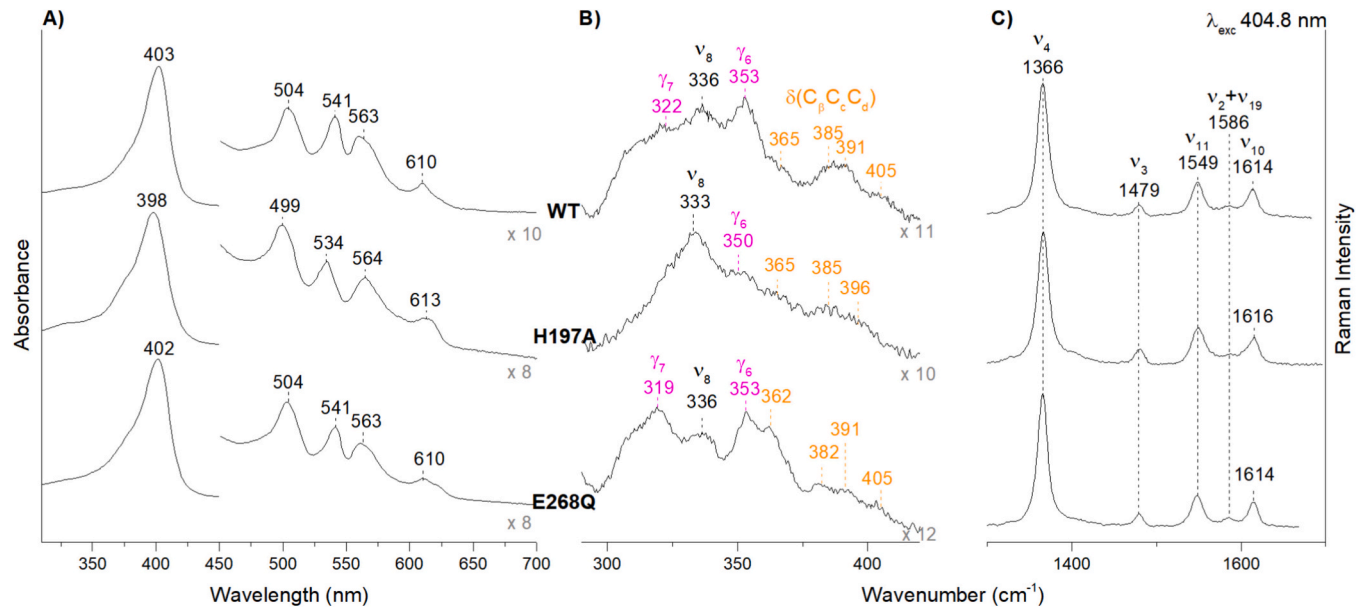

Fig. 7. (A) UV–vis absorption (solid lines), second derivative spectra (dotted lines, red), and RR spectra in the low (B) and high (C) wavenumber region of the cpIII - WT *Cd*CpfC and its E286Q, and H197A variants. The RR spectra have been obtained with the 404.8 nm excitation wavelength. In the low wavenumber region, the propionates bending modes $\delta(C_\beta C_c C_d)$ wavenumbers are indicated in orange and the out of plane modes in purple.

wavenumber region, due to the loss of the out-of plane mode at 322 (γ_7) and the intensity descrease of the γ_6 band, which also shifts from 353 to 350 cm^{-1} (Fig. 7B). Since these latter bands are activated by a porphyrin distortion, the doming deformation is markedly decreased in the H197A variant. This change may account for the blue-shift of the electronic absorption spectrum. In fact, based on several studies, it is generally accepted that a red-shift of the optical spectrum is the signature of porphyrin ring distortion [62–65].

The UV–vis and RR spectra of the coproheme – E286Q *Cd*CpfC complex are almost identical to that of the WT, typical of a 5cHS species (Fig. 8A) suggesting that, similarly to the cpIII complexes, the Glu286 mutation slightly affects the active site. On the contrary, the coproheme – H197A *Cd*CpfC complex is characterized by a broad Soret band centered at 399 nm, resolved in two minima at 397 nm and 404 nm in the second derivative (D^2) spectrum (Fig. 8A). These data suggest the presence of two different species, which are in fact clearly observed in the RR high-wavenumber region (Fig. 8C): a minor 6c low-spin (LS) species together with the main 5cHS species. Therefore, the His197A distal mutation alters the coproheme cavity, allowing internal strong ligands to bind the iron atom, both on the distal and the proximal sides. At the moment, the identity of these ligands have not been found. Further information on the effect of the mutation on the active site is given by the low wavenumber RR region (Fig. 8B), where a marked intensity decrease of the propionate $\delta(C_\beta C_c C_d)$ bending modes is

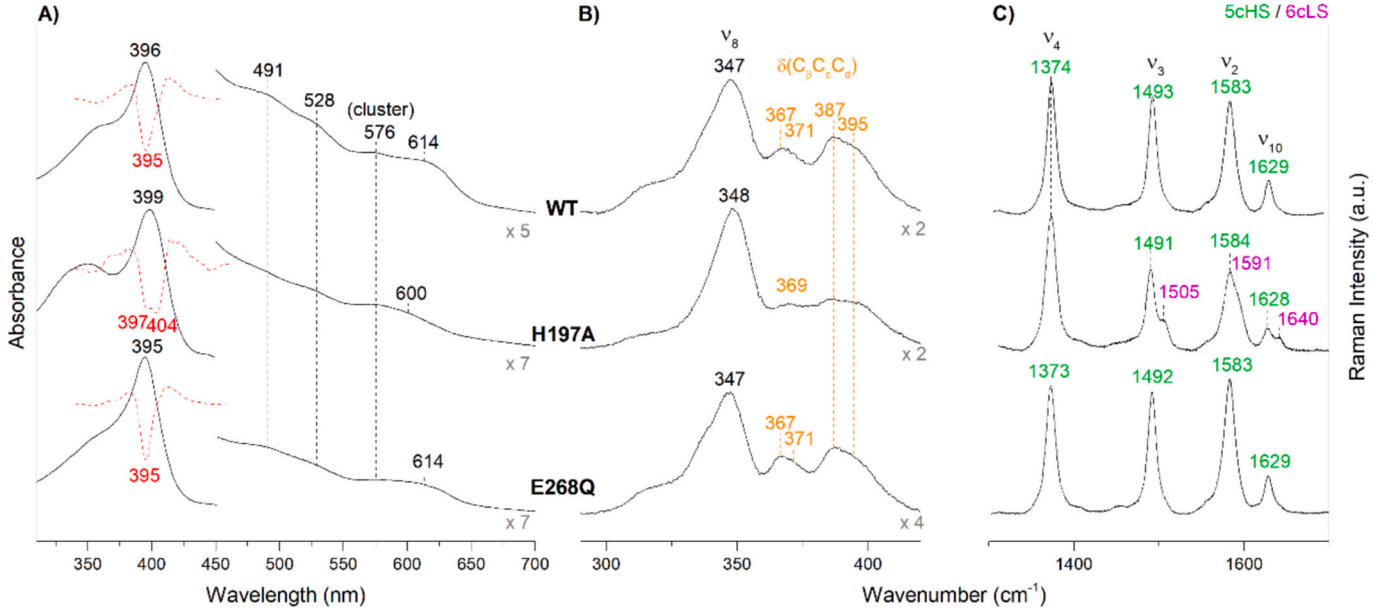

Fig. 8. (A) UV–vis absorption (solid lines), second derivative spectra (dotted lines, red), and RR spectra in the low (B) and high (C) wavenumber region of coproheme – WT *Cd*CpfC and its E286Q, and H197A variants. The RR spectra have been obtained with the 404.8 nm excitation wavelength. The wavenumbers of the RR core size marker bands are indicated in green for the 5cHS and purple for the 6cLS species, respectively. The propionates bending modes $\delta(C_\beta C_c C_d)$ wavenumbers are reported in orange.

observed, which may indicate a change of the propionate H-bond interactions with the polar residues of the protein pocket. Interestingly, in *Lm*CpfC the corresponding mutation of the distal His residues (H182A variant) allowed the entrance of a water molecule on the distal side of the iron atom, resulting in a minor hexacoordinated high spin (aquo 6cHS) population [66]. However, no changes in the intensity or the wavenumbers of the propionate bending modes $\delta(C_\beta C_c C_d)$ with respect to the WT *Lm*CpfC protein were observed [8].

3.6. Enzymatic activity: iron insertion and oxidation

The enzymatic insertion of ferrous iron into coproporphyrin III in presence of *Cd*CpfC was followed by UV–vis spectroscopy. In presence of 1.6 equivalents of iron, the absorption spectrum of cpIII – WT *Cd*CpfC complex completely shifts toward the coproheme-bound spectrum (Fig. 9A). The oxidation to ferric coproheme is instantaneous, as no formation of ferrous coproheme was detected. The iron insertion in cpIII – WT *Cd*CpfC complex follows biphasic behavior. Time traces were fitted double exponentially and only one of the phases, corresponding to k_{obs1}, shows a linear dependence on iron concentration, with $k_{on} = 78.91 \times 10^6\ M^{-1}\ s^{-1}$. By contrast, k_{obs2} does not show any concentration dependence (Fig. 9B) and therefore reflects an iron independent small structural effect within the active site.

Furthermore, also the activity of *Cd*CpfC E286Q (Fig. 9C) and H197A (Fig. 9E) mutants were monitored by UV–visible spectroscopy. End of titration was reached after addition of 6.5 and 4.5 equivalents of iron, respectively.

The final spectrum for E286Q mutant is almost identical to that obtained upon reconstitution of apo – E286Q *Cd*CpfC with coproheme (Fig. 8A, bottom), with the Soret band at 395 nm, Q bands at 491 and 528 nm and CT at 614 nm, but with a small amount of unreacted cpIII as evidenced by Q bands of the E286Q - cpIII complex. Accordingly, LC-ESI-MS analysis of porphyrin content (Fig. 9G) confirmed that the full conversion is not reached when the iron insertion is mediated by *Cd*CpfC E286Q, as 17% of coproporphyrin III is still present after incubation with 9 eq of iron. This behavior is not observed for the H197A mutant which catalyzes the reaction with a conversion rate comparable to the wild-type *Cd*CpfC. However, at the end of iron titration *Cd*CpfC H197A shows a Soret band centered at 399 nm, which is resolved in two minima at 397 and 404 nm in the second derivative (data not shown), suggesting the presence of a 5cHS form (397 nm) and a minor 6cLS species (shoulder at 404 nm), as observed in the coproheme complex (Fig. 8B, middle). In addition, the iron insertion in cpIII – E286Q and H197A *Cd*CpfC complexes follows a monophasic behavior. Time traces were fitted single exponentially and k_{obs}-values show a linear dependence on iron concentration, resulting in $k_{on} = 2.46 \times 10^2\ M^{-1}\ s^{-1}$ and $k_{on} = 0.894\ M^{-1}\ s^{-1}$, respectively (Fig. 9D, F).

4. Discussion

Coproporphyrin ferrochelatases from Firmicutes, which are predicted to be the most ancient CpfCs [27], efficiently catalyse the insertion of ferrous iron into coproporphyrin III [20,22–24]. Phylogenetic analyses with a focus on the binding motif sequences reveal that although most characterized actinobacterial representatives contain a [2Fe—2S] cluster, the majority is predicted not to [27]. Consequently, the ultimate question on the role of the iron-sulfur cluster in actinobacterial coproporphyrin ferrochelatases is unsolved, being evolutionary not conserved and not being relevant for catalysis.

Catalysis in firmicute CpfCs, which do not possess an iron sulfur cluster, is well described by in-solution spectroscopy, kinetic investigations, and also structural studies during turnover, revealing key porphyrin distortions [25,66]. These features are mediated and modulated by the direct interactions of active site amino acid residues and the propionate groups of coproporphyrin III. While the iron-sulfur cluster in human PpfC is potentially involved in dimer stabilization and/or protein-protein interactions [28–31,33] rather than in catalytic electron transfer [67], no such task is required for monomeric actinobacterial CpfCs. Moreover, in actinobacterial CpfCs the cluster is coordinated by residues on the C-terminal part of the protein, which is completely missing in firmicute CpfCs [27].

Here we have investigated the [2Fe—2S] in detail by RR spectroscopy and, in contrast to human PpfC, we observe a very stable cluster, also under oxygen environment. However, the type of the cluster, the nature of the ligands and the coordination motif are similar to those of human fC [29,68,69].

As the active site is concerned, the RR core size marker bands of the cpIII and coproheme complexes of WT *Cd*CpfC and WT *Lm*CpfC are in general very similar, even if the surrounding amino acid groups differ. This indicates that their central macrocyclic structure (the “core”) has very similar size, sharing structural features like planarity (coproheme) or non-planar distortions (doming in the cpIII), crucial for identifying their interactions within the protein scaffold. However, in the 300–400 cm^{-1} region the wavenumbers and intensities differences of the propionate bending modes suggest different H-bond strengths between the porphyrins and the proteins. These results, as shown by the overlay of the X-ray structures of the apo – WT *Cd*CpfC with the LmCpfC complexes, agree with the sequence alignment which revealed that not all residues involved in propionate H-bonding are conserved in the two proteins.

Interesting results have been obtained by studying the highly conserved His197/Glu286 pair. While no relevant effect has been observed upon replacing Glu286 with Gln, His197 residue has a preeminent role in stabilizing the active site. According to the X-ray structure which shows that in apo – WT *Cd*CpfC Glu286 and His197 are within H-bonding distance (2.9 Å), only the rupture of this interaction by replacing His197 with Ala affects the active site structure of both the cpIII and coproheme complexes. While the cpIII loses the doming deformation, in the absence of the His197 residue, in the coproheme complex the heme pocket is partially destabilized. In fact, alteration of the propionate H-bond interactions with the polar residues of the protein pocket is clearly observed in the RR spectra. In addition, coordination of internal strong ligands on both the proximal and the distal sides of the iron atom of coproheme occurs, resulting in the presence of a minor 6cLS species coexisting with the 5cHS native species. These results indicate that the active site structures of the cpIII and coproheme *Cd*CpfC complexes are different as compared to *Lm*CpfC. In fact, in *Lm*CpfC, where Glu263 is H-bonded to His182 residue in the cpIII but only partially involved in H-bond in the coproheme, the mutation of the His182 residue did not affect the cpIII complex [8,23]. On the other hand, in the coproheme complex the replacement of His182 with the small Ala residue, allowed a water molecule to enter into the distal side with the formation of a mixture of a 5cHS (WT-type) and an aquo 6cHS spin species [66].

Mutation of the distal residues, also affects the enzymatic activity. While, the final products obtained upon addtion of Fe^{2+} to the cpIII complexes are identical to the coproheme complexes obtained by directly complexing the proteins with coproheme, the end of titrations was reached after addition of higher amount of iron equivalents in the variants as compared to the WT. This discrepancy in affinity for the metal to the active site and subsequent insertion of ferrous iron is most probably related to changes in the active site access channel. The elimination of the negative charge by exchanging Glu286 with Gln potentially diminishes electrostatic attraction for Fe^{2+}. Exchange of His197 with Ala perturbs the acid-base equilibrium within the active site, resulting in the observed decrease of efficiency of iron insertion. In addition, at the end of the titration a small amount of unreacted E286Q-cpIII complex is still present.

The iron insertion in cpIII – WT *Cd*CpfC complex follows a biphasic behavior. Time traces were fitted double exponentially and only one of the phases, corresponding to k_{obs1}, shows a linear dependence on iron concentration, resulting in $k_{on} = 78.91 \times 10^6\ M^{-1}\ s^{-1}$. By contrast, k_{obs2}

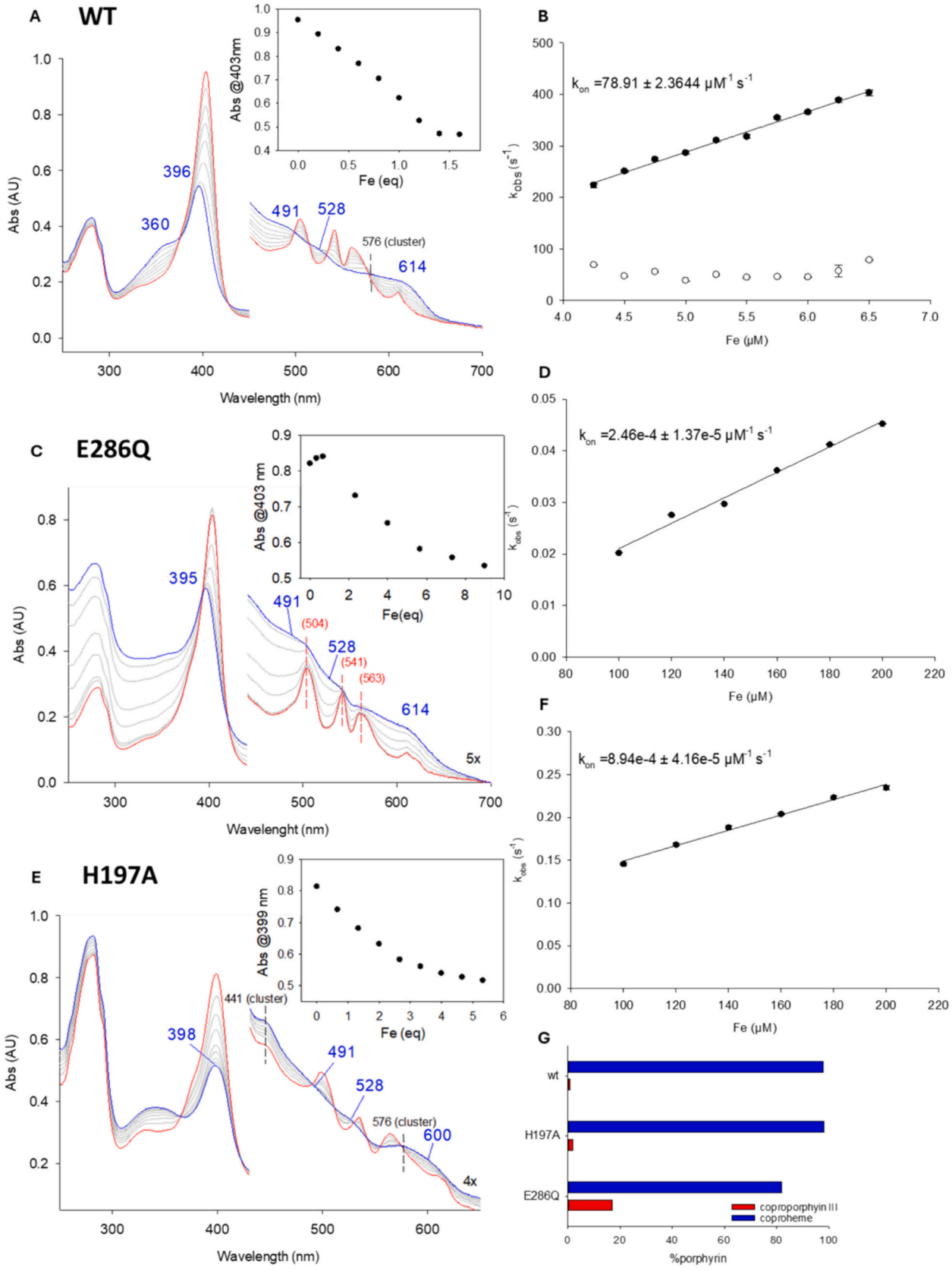

Fig. 9. Activity of WT *Cd*CpfC (A) and its E286Q (C), and H197A (E) variants followed by UV–vis absorption spectroscopy as cpIII - *Cd*CpfC complex (red trace) is titrated with ferrous iron to coproheme - *Cd*CpfC complex (blue trace). The inset shows the change in absorbance at 403 nm (WT, E286Q) or 399 nm (H197A) plotted versus the equivalent of ferrous iron added. Plots of k_{obs} versus iron concentration for WT *Cd*CpfC (B) and its E286Q (D), and H197A (F) variants for determination of the k_{on}. (G) Porphyrin content (%) determined by LC-ESI after iron titration for WT CdCpfC and its E286Q and H197A variants.

does not show any concentration dependency (Fig. 7B). On the contrary, the iron insertion in cpIII - *Cd*CpfC E286Q and H197A complexes follows a monophasic behavior. Time traces were fitted with a single exponential and the k_{obs} shows a linear dependence on iron concentration, resulting in $k_{on} = 2.46 \times 10^2\ M^{-1}\ s^{-1}$ and $k_{on} = 0.894\ M^{-1}\ s^{-1}$, respectively (Fig. 8D, F). These on-rates of the distal variants are significantly decreased compared to the WT *Cd*CpfC, highlighting their importance for catalysis. This is similar to what observed in *Lm*CpfC, where it was shown that especially the distal histidine variant is important for potentially deprotonating pyrrole nitrogen atoms and the glutamate residue is shaping the active site, being further involved in efficient oxidation of the ferrous iron to yield ferric coproheme [26]. The biphasic behavior of WT *Cd*CpfC can be explained by a small change of both the H-bond network and active site architecture after iron insertion, therefore being not dependent on the iron concentration. The loss of biphasic behavior agrees with an enlarged active site in the distal variants of *Cd*CpfC. With the aim to identify the entry site of the iron, the role of key active site residues has also been studied by computational methods in *Lm*CpfC and in human ferrochelatase. The data suggest an iron insertion from the site opposite of the distal Glu and His residues, emphasizing the role of the histidine in deprotonation of pyrrole nitrogens [67,70]. In future investigations we plan to study the role of the iron-sulfur cluster in more detail, in order to assess whether it is relevant for stabilizing the overall structure rather than for the catalytic activity. In fact, it appears to be unlikely that nature has evolved this rather energy costly tool for catalysis in these actinobacterial representatives when other homologous, like the more ancient firmicute enzymes, can perform the same reaction without a [2Fe—2S] cluster. No physiological role for other iron-sulfur cluster in proteins could be assigned yet, even after very thorough investigations, as for example in Asp1 pyrophosphatase from *S. pombe* [71] hosting a [2Fe—2S] cluster in vivo. Similarly to Asp1 pyrophosphatase, a role in electron transfer in *Cd*CpfC is unlikely, as the cluster is highly stable and cannot be reduced. Future studies will further investigate possible involvements of *Cd*CpfC in protein-protein interactions to shed light on potential regulatory tasks within heme biosynthesis.

CRediT authorship contribution statement

Alice Cassiani: Writing – original draft, Visualization, Investigation, Formal analysis, Data curation. **Thomas Gabler:** Writing – original draft, Visualization, Investigation, Formal analysis. **Andrea Dali:** Writing – original draft, Visualization, Investigation, Formal analysis, Data curation. **Paul G. Furtmüller:** Writing – review & editing, Resources. **Federico Sebastiani:** Writing – original draft, Visualization, Investigation, Formal analysis, Data curation. **Maurizio Becucci:** Writing – review & editing, Resources, Formal analysis. **Giulietta Smulevich:** Writing – original draft, Visualization, Supervision, Project administration, Funding acquisition, Conceptualization. **Stefan Hofbauer:** Writing – original draft, Validation, Supervision, Project administration, Funding acquisition, Formal analysis, Conceptualization.

Declaration of competing interest

The authors declare that they have no known competing financial interests or personal relationships that could have appeared to influence the work reported in this paper.

Acknowledgements

This research was funded by the Austrian Science Fund, FWF, projects P33544 (10.55776/P33544), P36967 (10.55776/P36967) (S.H.). Mass Spectrometry equipment was kindly provided by the BOKU Core Facility Mass Spectrometry, we thank the team of BOKU Core Facility Mass Spectrometry for conducting MS experiments. The equipment for drop-setting and crystal imaging as well as preparation for shipping of the crystals to the ESRF was kindly supported and provided by the BOKU Core Facility Biomolecular & Cellular Analysis (BmCA). The support of MUR-Italy ("Progetto Dipartimenti di Eccellenza 2023−2027, CUP B97G22000740001−DICUS 2.0, allocated to the Department of Chemistry "Ugo Schiff") is acknowledged (F.S., M.B., G.S.).

Appendix A. Supplementary data

Supplementary data to this article can be found online at https://doi.org/10.1016/j.ijbiomac.2026.152684.

Data availability

Data will be made available on request.

References

[1] I. Hamza, H.A. Dailey, One ring to rule them all: trafficking of heme and heme synthesis intermediates in the metazoans, Biochim. Biophys. Acta 1823 (9) (2012) 1617–1632.
[2] H.A. Dailey, et al., Prokaryotic heme biosynthesis: multiple pathways to a common essential product, Microbiol. Mol. Biol. Rev. 81 (1) (2017) e00048-16.
[3] H.A. Dailey, et al., Noncanonical coproporphyrin-dependent bacterial heme biosynthesis pathway that does not use protoporphyrin, Proc. Natl. Acad. Sci. 112 (7) (2015) 2210–2215.
[4] S. Bali, et al., Recent advances in the biosynthesis of modified tetrapyrroles: the discovery of an alternative pathway for the formation of heme and heme d 1, Cell. Mol. Life Sci. 71 (15) (2014) 2837–2863.
[5] M. Kühner, et al., The alternative route to heme in the methanogenic archaeon *Methanosarcina barkeri*, Archaea 2014 (1) (2014) 327637.
[6] G. Layer, Heme biosynthesis in prokaryotes, Biochim. Biophys. Acta, Mol. Cell Res. 1868 (1) (2021) 118861.
[7] N. Falb, et al., Structural aspects of enzymes involved in prokaryotic gram-positive heme biosynthesis, Comput. Struct. Biotechnol. J. 21 (2023) 3933–3945.
[8] T. Gabler, et al., Substrate specificity and complex stability of coproporphyrin ferrochelatase is governed by hydrogen-bonding interactions of the four propionate groups, FEBS J. 289 (6) (2022) 1680–1699.
[9] M. Zamocky, et al., The molecular evolution, structure, and function of coproporphyrinogen oxidase and protoporphyrinogen oxidase in prokaryotes, Biol.-Basel 12 (12) (2023).
[10] F. Sebastiani, et al., The role of the hydrogen bond network in maintaining heme pocket stability and protein function specificity of *C. diphtheriae* coproheme decarboxylase, Biomolecules 13 (2023) 235.
[11] G. Patil, et al., Reactivity of coproheme decarboxylase with monovinyl, monopropionate deuteroheme, Biomolecules 13 (2023) 946.
[12] F. Sebastiani, et al., Reaction intermediate rotation during the decarboxylation of coproheme to heme b in C. diphtheriae, Biophys. J. 120 (17) (2021) 3600–3614.
[13] C. Borelli, et al., In vivo porphyrin production by *P. acnes* in untreated acne patients and its modulation by acne treatment, Acta Derm. Venereol. 86 (4) (2006) 316–319.
[14] W. Kemmner, et al., Silencing of human ferrochelatase causes abundant protoporphyrin-IX accumulation in colon cancer, FASEB J. 22 (2) (2008) 500–509.
[15] J.D. Phillips, Heme biosynthesis and the porphyrias, Mol. Genet. Metab. 128 (3) (2019) 164–177.
[16] M. Hansson, L. Hederstedt, Purification and characterisation of a water-soluble ferrochelatase from *Bacillus subtilis*, Eur. J. Biochem. 220 (1) (1994) 201–208.
[17] M.D. Hansson, et al., Amino acid residues His183 and Glu264 in *Bacillus subtilis* ferrochelatase direct and facilitate the insertion of metal ion into protoporphyrin IX, Biochemistry 46 (1) (2007) 87–94.
[18] M.D. Hansson, et al., Bacterial ferrochelatase turns human: Tyr13 determines the apparent metal specificity of Bacillus subtilis ferrochelatase, J. Biol. Inorg. Chem. 16 (2) (2011) 235–242.
[19] D. Lecerof, et al., Structural and mechanistic basis of porphyrin metallation by ferrochelatase, J. Mol. Biol. 297 (1) (2000) 221–232.
[20] C. Hobbs, J.D. Reid, M. Shepherd, The coproporphyrin ferrochelatase of *Staphylococcus aureus*: mechanistic insights into a regulatory iron-binding site, Biochem. J. 474 (20) (2017) 3513–3522.
[21] S.A.L. Lobo, et al., Staphylococcus aureus haem biosynthesis: characterisation of the enzymes involved in final steps of the pathway, Mol. Microbiol. 97 (3) (2015) 472–487.
[22] S. Hofbauer, et al., Crystal structures and calorimetry reveal catalytically relevant binding mode of coproporphyrin and coproheme in coproporphyrin ferrochelatase, FEBS J. 287 (13) (2020) 2779–2796.
[23] A. Dali, et al., Active site architecture of coproporphyrin ferrochelatase with its physiological substrate coproporphyrin III: propionate interactions and porphyrin core deformation, Protein Sci. 32 (1) (2023) e4534.
[24] T. Gabler, et al., Iron insertion into coproporphyrin III-ferrochelatase complex: evidence for an intermediate distorted catalytic species, Protein Sci. 32 (2023) e4788.

[25] A. Dali, et al., Proximal ligand tunes active site structure and reactivity in bacterial L. monocytogenes coproheme ferrochelatase, Spectrochim. Acta A Mol. Biomol. Spectrosc. 313 (2024) 124120.
[26] T. Gabler, et al., Revisiting catalytic His and Glu residues in coproporphyrin ferrochelatase - unexpected activities of active site variants, FEBS J. 291 (2024) 2260–2272.
[27] R.S. Weerth, A.E. Medlock, H.A. Dailey, Ironing out the distribution of [2Fe-2S] motifs in ferrochelatases, J. Biol. Chem. 297 (5) (2021) 101017.
[28] H.A. Dailey, M.G. Finnegan, M.K. Johnson, Human ferrochelatase is an iron-sulfur protein, Biochemistry 33 (2) (1994) 403–407.
[29] C.K. Wu, et al., The 2.0 A structure of human ferrochelatase, the terminal enzyme of heme biosynthesis, Nat. Struct. Biol. 8 (2) (2001) 156–160.
[30] B.R. Crouse, et al., Site-directed mutagenesis and spectroscopic characterization of human ferrochelatase: identification of residues coordinating the [2Fe-2S] cluster, Biochemistry 35 (50) (1996) 16222–16229.
[31] H.A. Dailey, V.M. Sellers, T.A. Dailey, Mammalian ferrochelatase. Expression and characterization of normal and two human protoporphyric ferrochelatases, J. Biol. Chem. 269 (1) (1994) 390–395.
[32] V.M. Sellers, M.K. Johnson, H.A. Dailey, Function of the [2FE-2S] cluster in mammalian ferrochelatase: a possible role as a nitric oxide sensor, Biochemistry 35 (8) (1996) 2699–2704.
[33] M. Shepherd, Tamara, Harry, A new class of [2Fe-2S]-cluster-containing protoporphyrin (IX) ferrochelatases, Biochem. J. 397 (1) (2006) 47–52.
[34] T.A. Dailey, H.A. Dailey, Identification of [2Fe-2S] clusters in microbial ferrochelatases, J. Bacteriol. 184 (9) (2002) 2460–2464.
[35] L. Castro, et al., Aconitases: non-redox iron-sulfur proteins sensitive to reactive species, Acc. Chem. Res. 52 (9) (2019) 2609–2619.
[36] B. Blanc, C. Gerez, S. Ollagnier de Choudens, Assembly of Fe/S proteins in bacterial systems: biochemistry of the bacterial ISC system, Biochim. Biophys. Acta 1853 (6) (2015) 1436–1447.
[37] D.W. Bak, E. Weerapana, Proteomic strategies to interrogate the Fe-S proteome, Biochim. Biophys. Acta, Mol. Cell Res. 1871 (7) (2024) 119791.
[38] S. Hofbauer, et al., Structure and heme-binding properties of HemQ (chlorite dismutase-like protein) from listeria monocytogenes, Arch. Biochem. Biophys. 574 (2015) 36–48.
[39] T.C. Terwilliger, et al., Iterative model building, structure refinement and density modification with the PHENIX AutoBuild wizard, Acta Crystallogr. D Biol. Crystallogr. 64 (Pt 1) (2008) 61–69.
[40] P. Emsley, et al., Features and development of Coot, Acta Crystallogr. D Biol. Crystallogr. 66 (Pt 4) (2010) 486–501.
[41] P.D. Adams, et al., PHENIX: a comprehensive Python-based system for macromolecular structure solution, Acta Crystallogr. D Biol. Crystallogr. 66 (Pt 2) (2010) 213–221.
[42] S. French, K. Wilson, On the treatment of negative intensity observations, Acta Crystallogr. A34 (1978) 517–525.
[43] V.B. Chen, et al., MolProbity: all-atom structure validation for macromolecular crystallography, Acta Crystallogr. D Biol. Crystallogr. 66 (Pt 1) (2010) 12–21.
[44] S. Hofbauer, et al., Hydrogen peroxide-mediated conversion of coproheme to heme b by HemQ-lessons from the first crystal structure and kinetic studies, FEBS J. 283 (23) (2016) 4386–4401.
[45] A.E. Medlock, et al., A pi-helix switch selective for porphyrin deprotonation and product release in human ferrochelatase, J. Mol. Biol. 373 (4) (2007) 1006–1016.
[46] Z. Mao, et al., Cluster-dependent charge-transfer dynamics in iron–sulfur proteins, Biochemistry 57 (6) (2018) 978–990.
[47] L. Valer, et al., Methods to identify and characterize iron-sulfur oligopeptides in water, Can. J. Chem. 100 (7) (2022) 475–483.
[48] A. Kubas, Characterization of charge transfer excited states in [2Fe–2S] iron–sulfur clusters using conventional configuration interaction techniques, Theor. Chem. Accounts 139 (7) (2020) 120.
[49] G. Caserta, et al., Unusual structures and unknown roles of FeS clusters in metalloenzymes seen from a resonance Raman spectroscopic perspective, Coord. Chem. Rev. 452 (2022).
[50] T.G. Spiro, R.S. Czernuszewicz, Resonance Raman spectroscopy of metalloproteins, Methods Enzymol. 246 (1995) 416–460.
[51] L.K. Kilpatrick, et al., Cluster structure and H-bonding in native, substrate-bound, and 3fe forms of aconitase as determined by resonance Raman-spectroscopy, J. Am. Chem. Soc. 116 (9) (1994) 4053–4061.
[52] D. Rossetto, et al., Protocellular heme and iron-sulfur clusters, Acc. Chem. Res. 57 (16) (2024) 2293–2302.
[53] S. Han, R.S. Czernuszewicz, T.G. Spiro, Vibrational-spectra and normal mode analysis for [2fe-2s] protein analogs using S-34, Fe-54, and H-2 substitution - coupling of Fe-S stretching and S-C-C bending modes, J. Am. Chem. Soc. 111 (10) (1989) 3496–3504.
[54] R.S. Czernuszewicz, et al., Vibrational-mode structure and symmetry in proteins and analogs containing Fe4s4 clusters - resonance Raman evidence for different degrees of distortion in Hipip and ferredoxin, J. Am. Chem. Soc. 109 (23) (1987) 7178–7187.
[55] S. Todorovic, M. Teixeira, Resonance Raman spectroscopy of Fe-S proteins and their redox properties, J. Biol. Inorg. Chem. 23 (4) (2018) 647–661.
[56] S. Han, et al., Fe2S2 protein resonance Raman spectra revisited: structural variations among adrenodoxin, ferredoxin, and red paramagnetic protein, J. Am. Chem. Soc. 111 (10) (1989) 3505–3511.
[57] D. Kuila, et al., Resonance Raman studies of Rieske-type proteins, Biochim. Biophys. Acta 1140 (2) (1992) 175–183.
[58] J. Meyer, et al., Mutated forms of the [2Fe-2S] ferredoxin from *Clostridium pasteurianum* with noncysteinyl ligands to the iron-sulfur cluster, Biochemistry 33 (46) (1994) 13642–13650.
[59] W. Fu, et al., Resonance Raman and magnetic circular dichroism studies of reduced [2Fe-2S] proteins, J. Biol. Chem. 267 (22) (1992) 15502–15510.
[60] R.S. Czernuszewicz, et al., Resonance Raman-spectra of rubredoxin - new assignments and vibrational coupling mechanism from Fe-54 Fe-56 isotope shifts and variable-wavelength excitation, Inorg. Chem. 25 (5) (1986) 696–700.
[61] T.F. Tirrell, et al., Resonance Raman studies of the (his)(Cys)3 2Fe-2S cluster of MitoNEET: comparison to the (Cys)4 mutant and implications of the effects of pH on the labile metal center, Biochemistry 48 (22) (2009) 4747–4752.
[62] J. Shelnutt, C. Medforth, Nonplanar porphyrins and their significance in proteins, Chem. Soc. Rev. 27 (1) (1998) 31–42.
[63] A.K. Wertsching, A.S. Koch, S.G. DiMagno, On the negligible impact of ruffling on the electronic spectra of porphine, tetramethylporphyrin, and perfluoroalkylporphyrins, J. Am. Chem. Soc. 123 (17) (2001) 3932–3939.
[64] X.Z. Song, et al., Representation of nonplanar structures of nickel(II) 5,15-disubstituted porphyrins in terms of displacements along the lowest-frequency normal coordinates of the macrocycle, J. Am. Chem. Soc. 118 (51) (1996) 12975–12988.
[65] M.W. Grinstaff, et al., Structures, electronic-properties, and oxidation-reduction reactivity of halogenated iron porphyrins, Inorg. Chem. 34 (19) (1995) 4896–4902.
[66] A. Dali, et al., Entrance channels to coproheme in coproporphyrin ferrochelatase probed by exogenous imidazole binding, J. Inorg. Biochem. 260 (2024) 112681.
[67] J. Wu, et al., Human ferrochelatase: insights for the mechanism of ferrous iron approaching protoporphyrin IX by QM/MM and QTCP free energy studies, J. Chem. Inf. Model. 56 (12) (2016) 2421–2433.
[68] H.A. Dailey, et al., Ferrochelatase at the millennium: Structures, mechanisms and [2Fe-2S] clusters, Cell. Mol. Life Sci. 57 (13–14) (2000) 1909–1926.
[69] A.E. Medlock, et al., Insight into the function of active site residues in the catalytic mechanism of human ferrochelatase, Biochem. J. 478 (17) (2021) 3239–3252.
[70] Y. Lin, Y. Shen, An automatic pathway searching strategy in enzyme catalysis: a case study of LmCpfC, Chemphyschem 26 (23) (2025) e202500515.
[71] H. Rosenbach, et al., The Asp1 pyrophosphatase from *S. pombe* hosts a [2Fe-2S](2+) cluster in vivo, J. Biol. Inorg. Chem. 26 (1) (2021) 93–108.